Regulation of microtubule-associated motors drives intermediate filament network polarization

Cécile Leduc and Sandrine Etienne-Manneville

Institut Pasteur Paris, Cell Polarity, Migration and Cancer Unit, UMR 3691, Equipe Labellisée Ligue Contre le Cancer, Centre National de la Recherché Scientifique, 75724 Paris, France.

Intermediate filaments (IFs) are key players in the control of cell morphology and structure as well as in active processes such as cell polarization, migration, and mechanoresponses. However, the regulatory mechanisms controlling IF dynamics and organization in motile cells are still poorly understood. In this study, we investigate the mechanisms leading to the polarized rearrangement of the IF network along the polarity axis. Using photobleaching and photoconversion experiments in glial cells expressing vimentin, glial fibrillary acidic protein, and nestin, we show that the distribution of cytoplasmic IFs results from a continuous turnover based on the cooperation of an actin-dependent retrograde flow and anterograde and retrograde microtubule-dependent transports. During wound-induced astrocyte polarization, IF transport becomes directionally biased from the cell center toward the cell front. Such asymmetry in the transport is mainly caused by a Cdc42- and atypical PKC–dependent inhibition of dynein-dependent retrograde transport. Our results show how polarity signaling can affect the dynamic turnover of the IF network to promote the polarization of the network itself.

Introduction

Cell polarity is essential for most cell functions, including cell division, cell differentiation, and cell migration. Its fundamental role in pluricellular organisms is highlighted by the fact that perturbation of cell polarity is a hallmark of cancer cells. Polarity is controlled by environmental cues, that lead to the structural and functional organization of its components along a so-called polarity axis. The small GTPase Cdc42 has been shown to play a key role in the signaling cascade, leading to cell polarization in a wide variety of cell types and cellular functions (Etienne-Manneville, 2004). Changes in the microenvironment can modify the polarity axis to promote new polarized functions such as directed migration (Etienne-Manneville, 2004). To initiate migration, cells undergo a front–rear polarization with the formation of a protrusive front and a retracting rear (Etienne-Manneville, 2004; Llense and Etienne-Manneville, 2015; Ladoux et al., 2016). Cell polarization is associated with a dramatic reorganization of the cytoskeletal filamentous networks. The organization of actin filaments, which triggers the generation of protrusive forces at the cell front and contractile forces at the cell rear, has been extensively described (Carlier et al., 2015; Köster and Mayor, 2016). During front–rear polarization, the microtubule network reorients and elongates in the direction of migration to orchestrate the asymmetric distribution of organelles and membrane traffic and the dynamics of cellular adhesions (Etienne-Manneville, 2013). The role of the microtubule network is particularly evident in astrocytes, major glial cells of the central nervous system, which migrate collectively during development (Gnanaguru et al., 2013) and also in the adult in response to inflammatory situations (Sofroniew, 2009). In these cells, the polarized reorganization of the microtubule network relies on Cdc42, which acts via its downstream effector Par6, and atypical PKC (aPKC) to locally control microtubule cortical anchoring at the cell front and centrosome reorientation (Etienne-Manneville et al., 2005; Manneville et al., 2010).

Like microfilaments and microtubules, intermediate filaments (IFs) have been shown to participate in directed cell migration (Lepekhin et al., 2001; Dupin et al., 2011; Sakamoto et al., 2013; Leduc and Etienne-Manneville, 2015; Gan et al., 2016) as well as in cancer cell invasion (Leduc and Etienne-Manneville, 2015). Depletion and disassembly of type III vimentin slows down fibroblast migration (Helfand et al., 2011). In particular, vimentin modulates lamellipodia formation (Helfand et al., 2011) and influences the organization of both actin and microtubules (Shabbir et al., 2014; Huber et al., 2015; Jiu et al., 2015). Microtubule–vimentin IF linkers include molecular motors such as kinesin-1 (Gyoeva and Gelfand, 1991; Liao and Gundersen, 1998; Prahlad et al., 1998) and cytoplasmic dynein (Helfand et al., 2002), cytoskeletal cross-linkers like plectin (Svitkina et al., 1996), and the tumor suppressor adenomatous polyposis coli (Sakamoto et al., 2013). IFs are also key

Correspondence to Sandrine Etienne-Manneville: setienne@pasteur.fr

Abbreviations used: aPKC, atypical PKC; DHC, dynein heavy chain; GFAP, glial fibrillary acidic protein; IF, intermediate filament; KHC, kinesin heavy chain; N-WASp, Neural–Wiskott Aldrich Syndrome protein; siKHC, small interfering KHC; STORM, stochastic optical reconstitution microscopy.

The Rockefeller University Press $30.00
J. Cell Biol. Vol. 216 No. 6 1689–1703
https://doi.org/10.1083/jcb.201607045

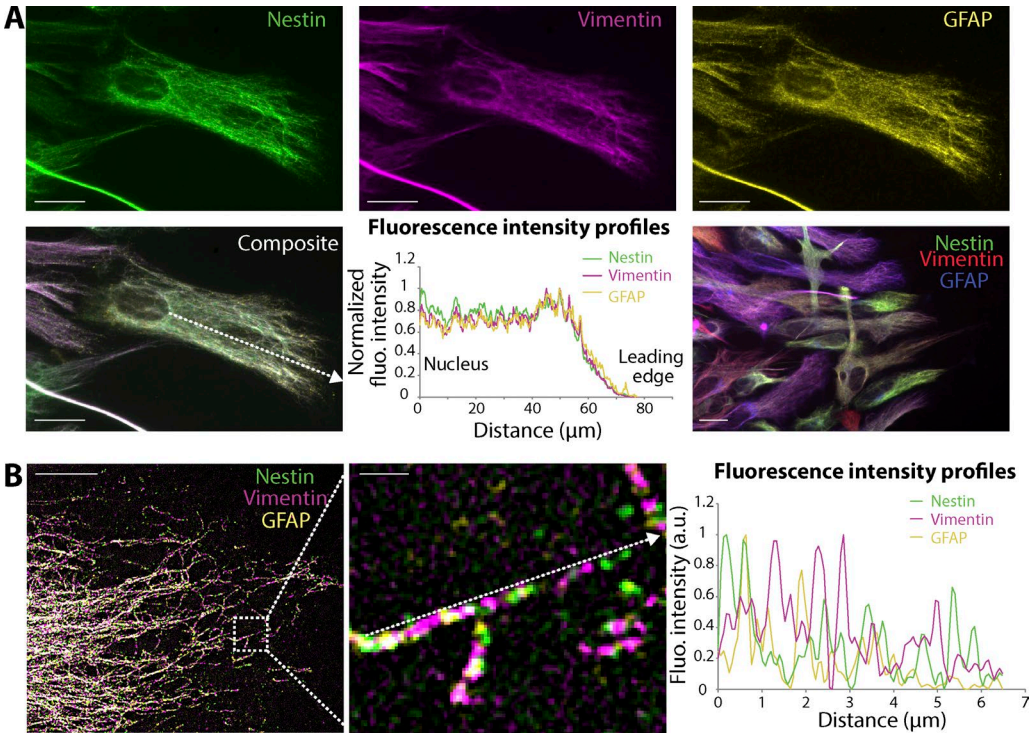

Figure 1. **Distribution of cytoplasmic IFs in astrocytes.** (A) Epifluorescence image of nestin (green), vimentin (magenta), and GFAP (yellow) immunostaining of a migrating astrocyte 10 h after wounding. The intensity profiles were obtained along the dotted arrow. Bars, 20 µm. (B) 3D structured illumination microscopy images of nestin (green), vimentin (magenta), and GFAP (yellow) immunostaining at the front of a migrating astrocyte. Kinesin depletion was used to decrease the density of IFs at the cell front, facilitating the visualization of single filaments. A higher magnification of the boxed region is shown in the middle. Fluorescence (Fluo.) intensity profiles showing the distribution of nestin, vimentin, and GFAP along a single filament (indicated by a dotted arrow in the inset) are shown on the right. Bars: (main image) 10 µm; (inset) 1 µm. a.u., arbitrary units.

players in the establishment and maintenance of cell polarity and directed movement (Dupin et al., 2011; Shabbir et al., 2014; Gan et al., 2016). IFs are necessary for astrocyte-directed migration both in vivo and in vitro (Lepekhin et al., 2001; Dupin et al., 2011). Astrocytes and astrocytoma cells essentially express vimentin, glial fibrillary acidic protein (GFAP), nestin, and possibly synemin (Hol and Pekny, 2015). The integrity of the astrocytic IF network is required for correct nuclear positioning, microtubule organization, and cell polarity (Dupin and Etienne-Manneville, 2011).

IF functions during migration are associated with the reorganization of the IF network along the front–rear polarity axis (Dupin et al., 2011; Sakamoto et al., 2013; Shabbir et al., 2014; Gan et al., 2016). IF organization generally depends on the microtubule network integrity (Goldman, 1971) and actin retrograde flow (Hollenbeck et al., 1989). Recent studies showed that vimentin precursors and also vimentin mature filaments are transported in a microtubule-dependent manner (Robert et al., 2014, 2016; Hookway et al., 2015). Moreover, vimentin IFs have been shown to reorganize by severing and reannealing (Çolakoğlu and Brown, 2009; Hookway et al., 2015) as observed for neurofilaments (Uchida et al., 2013). Although IF network reorganization may result from a contribution of the movement of filament precursors, squiggles, and mature filaments, the relative contribution of these different movements in the steady-state dynamics of the IF network and their regulation during the polarized reorganization of the IF network in migrating cells is still unclear.

In this study, we first investigate the mechanisms triggering IF turnover in motile astrocytoma cells, which undergo a nondirected and nonpersistent migration. Then, we use a scratch assay to trigger the persistent directed migration of primary rat astrocytes in a time-controlled manner and identify the key regulatory processes driving IF rearrangement during cell polarization (Etienne-Manneville, 2006). Our results show that the dynamics of the IF network mainly involve a combination of microtubule- and actin-driven transport of IFs and that the control of IF transport is locally controlled by Cdc42 to promote the front–rear polarization of the IF network during wound-induced astrocyte migration.

Results

IF dynamics in motile cells

To investigate the dynamics of type III IFs, we first used astrocytoma U373 cells, which are highly motile cells, undergoing random migration in the absence of any stimulus. Glial cells express vimentin, GFAP, and nestin in a dense filament network. Immunostaining of nestin, vimentin, and GFAP showed that the relative expression of each IF protein changes from one cell to another, but all have similar distribution inside the cytoplasm (Fig. 1 A). When all were expressed, the three IF proteins colocalized in cytoplasmic IFs (Fig. 1 A), with >98% colocalization between vimentin/nestin and vimentin/GFAP, confirming that the three IF proteins copolymerize in astrocytes (Eliasson et al., 1999). However, multicolor structured illumination microscopy showed that the three IF proteins, which were all present in each single filament, formed distinct subdomains that partially overlap (Fig. 1 B).

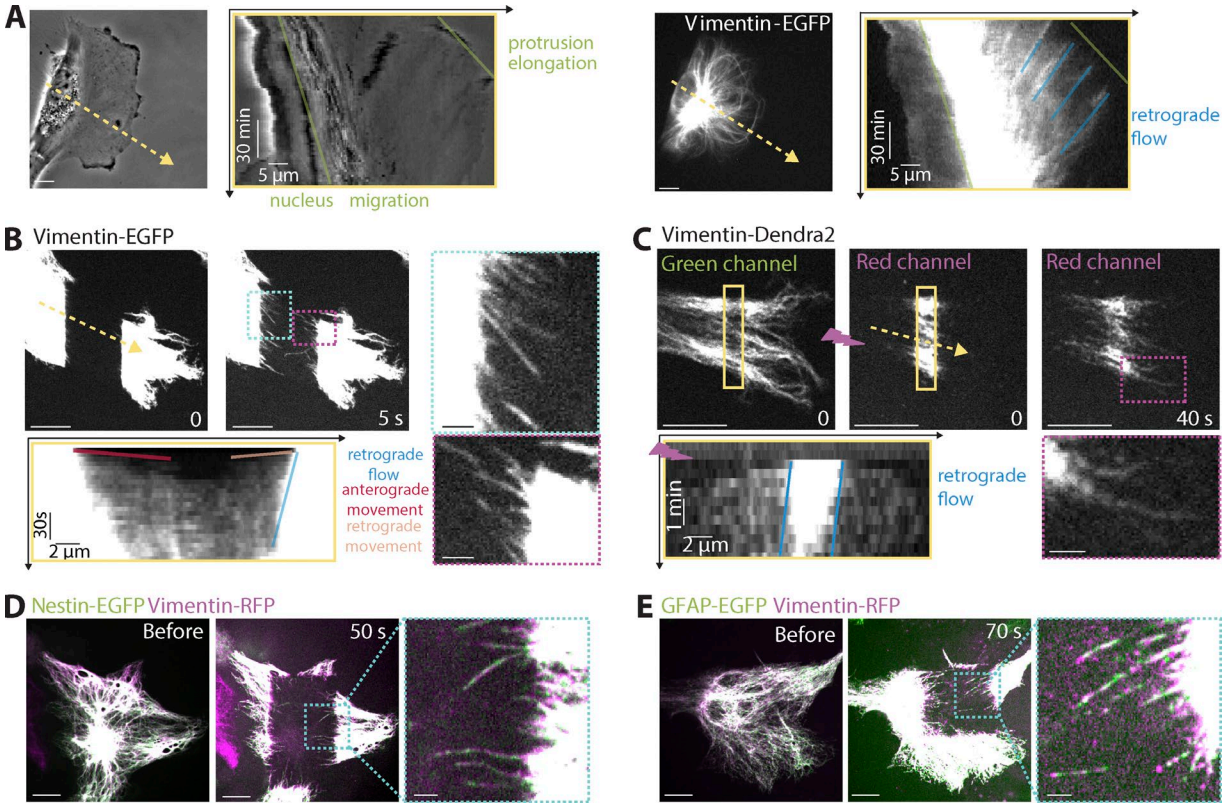

Figure 2. **Vimentin filament dynamics during astrocytoma random migration.** (A) Phase contrast (left) and fluorescence (right) images of a motile astrocytoma cell (U373 cell line) expressing vimentin-EGFP (Video 1; total time, 120 min). (B) Still images of the vimentin network acquired 0 and 5 s after photobleaching of a vimentin-GFP– and tubulin-mCherry–expressing astrocytoma cell (Video 2; total time, 2 min; see also Fig. S1, B–D). mCherry-tubulin images are shown in Fig. S1 C. (C) Green and red fluorescence images of a vimentin-Dendra2–expressing astrocytoma cell just after (t = 0) and 40 s after photoconversion by a 405-nm flash illumination (purple) in the yellow rectangle (Video 3; total time, 2 min). Kymographs are boxed in yellow and show the fluorescence intensity profile along the yellow arrow in the corresponding image over time. The colored lines highlight the nucleus and protrusion forward movements (green), the retrograde flow (blue), and the anterograde (red) and retrograde (orange) movements of IFs on kymographs. The higher-magnification images of regions indicated by a cyan or purple dashed box are shown in the corresponding dotted line boxes. (D) Merged images of an astrocytoma coexpressing GFAP-EGFP and vimentin-RFP just before and 50 s after photobleaching with a zoom on moving filaments. (E) Merged images of an astrocytoma coexpressing nestin-EGFP and vimentin-RFP just before and 70 s after photobleaching with a zoom on filaments. Bars: (main images) 10 µm; (insets) 2 µm.

To investigate the dynamics of cytoplasmic IFs, we first used astrocytoma cells expressing vimentin-EGFP. Time-lapse video microscopy showed a constant deployment of filaments in the cell protrusive regions along with a global retrograde flow of IF bundles converging toward the nucleus (Fig. 2 A and Video 1). To investigate the mechanisms involved in the dynamics of the vimentin-EGFP, we performed FRAP experiments (Fig. 2 B and Video 2). After bleaching of vimentin-EGFP, the total fluorescence inside the bleached area increased linearly with time (Fig. S1, A and B). It originated from the rest of the cell, with the total fluorescence of the cell remaining constant (Fig. S1 A). This was strikingly different from the recovery of mCherry-tubulin fluorescence, which increased exponentially with time (as previously observed by Walczak et al. [2010]) and displayed a uniform distribution inside the bleached region (Fig. S1, C and D). The global retrograde flow of vimentin IFs was observed by a slow shift of the photobleached region toward the cell rear (Fig. 2 B, blue line on the kymograph; velocity of ~0.009 µm/s). We also observed a faster but more limited fluorescence recovery from the edges of the bleached region (indicated by red and orange lines on the kymograph; Fig. 2 B). The image acquired 5 s after photobleaching showed that this fast fluorescence recovery resulted from single vimentin filaments coming either from the cell periphery (retrograde movement at ~0.52 µm/s) or from the cell center (anterograde movement at ~0.50 µm/s; Fig. 2 B). We could not detect any polymerization in the photobleached area and thus concluded that at this time scale (<1 h), turnover of the vimentin-EGFP mainly results from the movement of preexisting filaments rather than from polymerization or annealing. These results were confirmed by local photoconversion from green to red of vimentin-Dendra2 (Fig. 2 C and Video 3). Photoconverted vimentin was only present in filaments emerging from the photoconverted region. Vimentin transport was also observed in mouse embryonic fibroblasts, where there is only one type of IF protein (vimentin) expressed (Fig. S1 E). We then investigated whether nestin and GFAP behave similarly to vimentin. FRAP experiments on cells expressing any two fluorescent IF proteins showed that both proteins included in the same filament were transported together in the photobleached area (Fig. 2, D and E). These observations show that vimentin, nestin, and GFAP are found together in IFs and display identical dynamics. We thus used vimentin-EGFP as a marker of the entire astrocyte IF network.

IF interplay with actin filaments and microtubules

To determine how IF dynamics are coupled to the other cytoskeletal structures, astrocytoma cells were cotransfected with

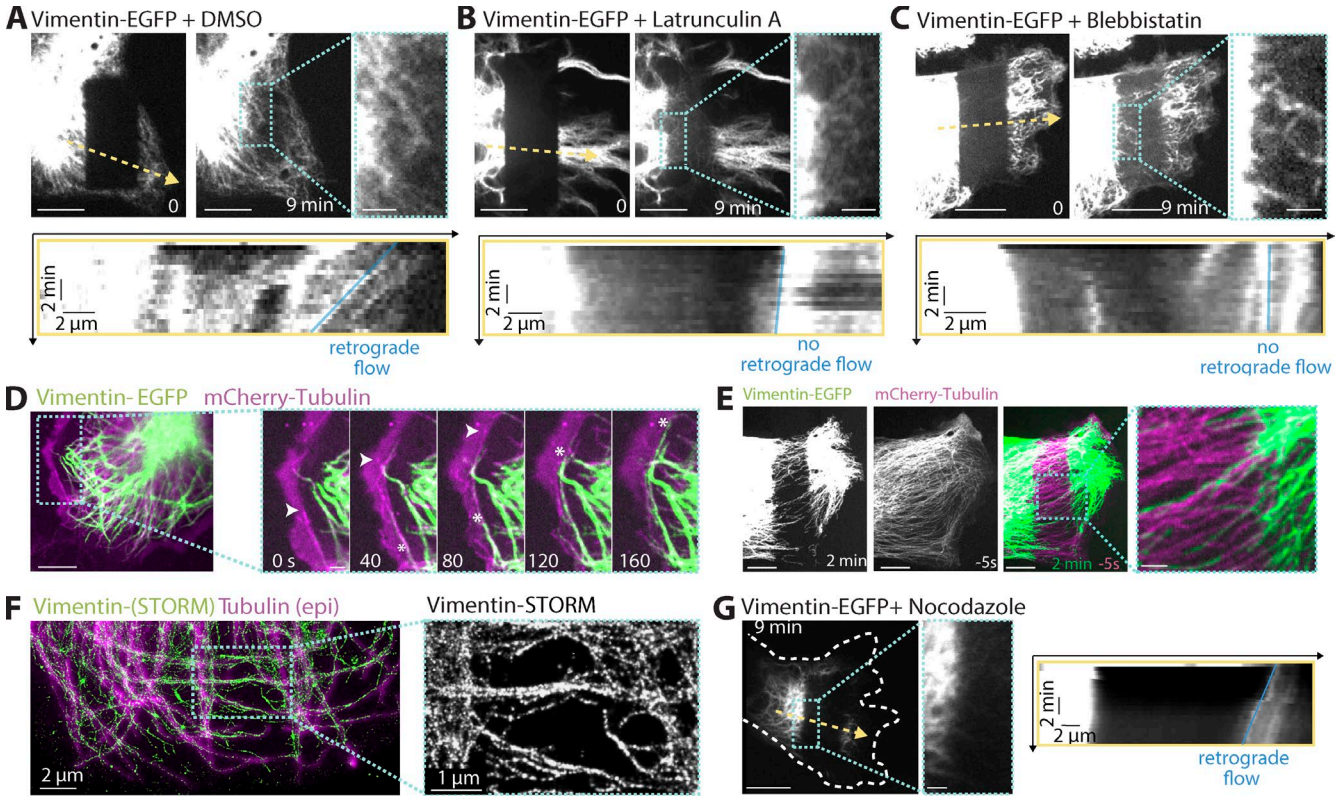

Figure 3. **Vimentin interplay with actin filaments and microtubules.** (A–C) Fluorescence images taken from FRAP experiments on vimentin-EGFP–expressing astrocytoma cells treated with DMSO (A), 10 µM latrunculin A (B), and 2 µM blebbistatin (C). The images were acquired 0 and 9 min after photobleaching. Kymographs are boxed in yellow and show the fluorescence intensity profile along the yellow arrows in the corresponding images over time for each condition. The higher-magnification images of regions indicated by a blue dotted box are shown in the corresponding dotted line boxes. (D) Fluorescence image of an astrocytoma cell expressing vimentin-EGFP (green) and mCherry-tubulin (magenta). Time-lapse images of the region indicated by a dotted blue box are shown on the right. Arrowheads highlight a microtubule tip, and asterisks show the tip of a vimentin IF moving along this microtubule (Video 5; total time, 12 min). (E) Fluorescence images of an astrocytoma cell expressing vimentin-EGFP and mCherry-tubulin showing EGFP fluorescence 2 min after photobleaching and mCherry fluorescence before photobleaching. The merged image and the higher-magnification image of the boxed region are shown on the right. (F) STORM image of the edge of a migrating astrocytoma cell stained for vimentin (green) merged with the corresponding epifluorescence (epi) image of the microtubule network (magenta). A higher magnification of the region indicated by a dotted line rectangle on the vimentin network is shown on the right. (G) FRAP experiment on a vimentin-EGFP–expressing astrocytoma cell treated with 10 µM nocodazole. White dashed outline indicates the cell contour. A higher magnification of the boxed region (cyan) shows single vimentin filaments moving into the bleached area from the adjacent regions. The kymograph shows the fluorescence intensity profile along the yellow arrow over time. Bars: (main images) 10 µm; (insets) 2 µm; unless otherwise indicated.

vimentin-EGFP and Lifeact-mCherry that label both vimentin and actin filaments (Fig. S2 A and Video 4). Vimentin bundles and actin transverse arcs underwent a similar retrograde flow (Fig. 2 A; highlighted by a blue line on the kymograph) with a velocity of ∼0.006 µm/s, which is identical to that of actin fibers in other cell types (Dupin et al., 2011; Jiu et al., 2015). Actin depolymerization by latrunculin A or myosin II inhibition with blebbistatin blocked the IF retrograde flow (Fig. 3, A–C). However, these inhibitors did not prevent the emergence of fast-moving IFs from the edges of the photobleached area (Fig. 3, A–C), indicating that there is a bulk retrograde flow superimposed on the individual transport movements. Two-color live-cell imaging of vimentin-EGFP and mCherry-tubulin showed that vimentin IFs elongate along microtubules both at the periphery (Fig. 3 D and Video 5) and inside the cell when probed by FRAP (Fig. 3 E). The organization of vimentin filaments around microtubules was confirmed by stochastic optical reconstitution microscopy (STORM; Fig. 3 F). Microtubule depolymerization with nocodazole totally blocked the emergence of fast-moving IFs from the edges of the photobleached area but did not affect the slow actin-dependent retrograde flow (Fig. 3 G). Together with the global actin-dependent slow retrograde flow, these microtubule-dependent transport mechanisms are the main regulators of IF network turnover in motile cells.

Regulation of kinesin-1– and dynein-1–dependent transport drives the polarization of the IF network

Astrocytoma cells migrate in a random manner without any steady defined polarity, making the study of cell polarization difficult. Therefore, we used an in vitro wound healing assay to control the timing and the direction of polarization of primary astrocytes and to investigate how cell polarization affects the IF network organization. Wounding of the astrocyte monolayer induces the polarization of the cells on the wound edge with the establishment of a stable front–rear polarity axis perpendicular to the initial wound (Etienne-Manneville and Hall, 2001; Etienne-Manneville, 2006). We observed that after wounding, the morphological changes of the leading cells correlated with the anisotropic reorganization of the IF network along the polarity axis (Fig. 4 A and Video 6). Transient transfection of vimentin-EGFP in astrocytes induced the expression of the tagged protein to a level corresponding with ∼10% of that of endogenous vimentin (measured by Western blot with a transfection

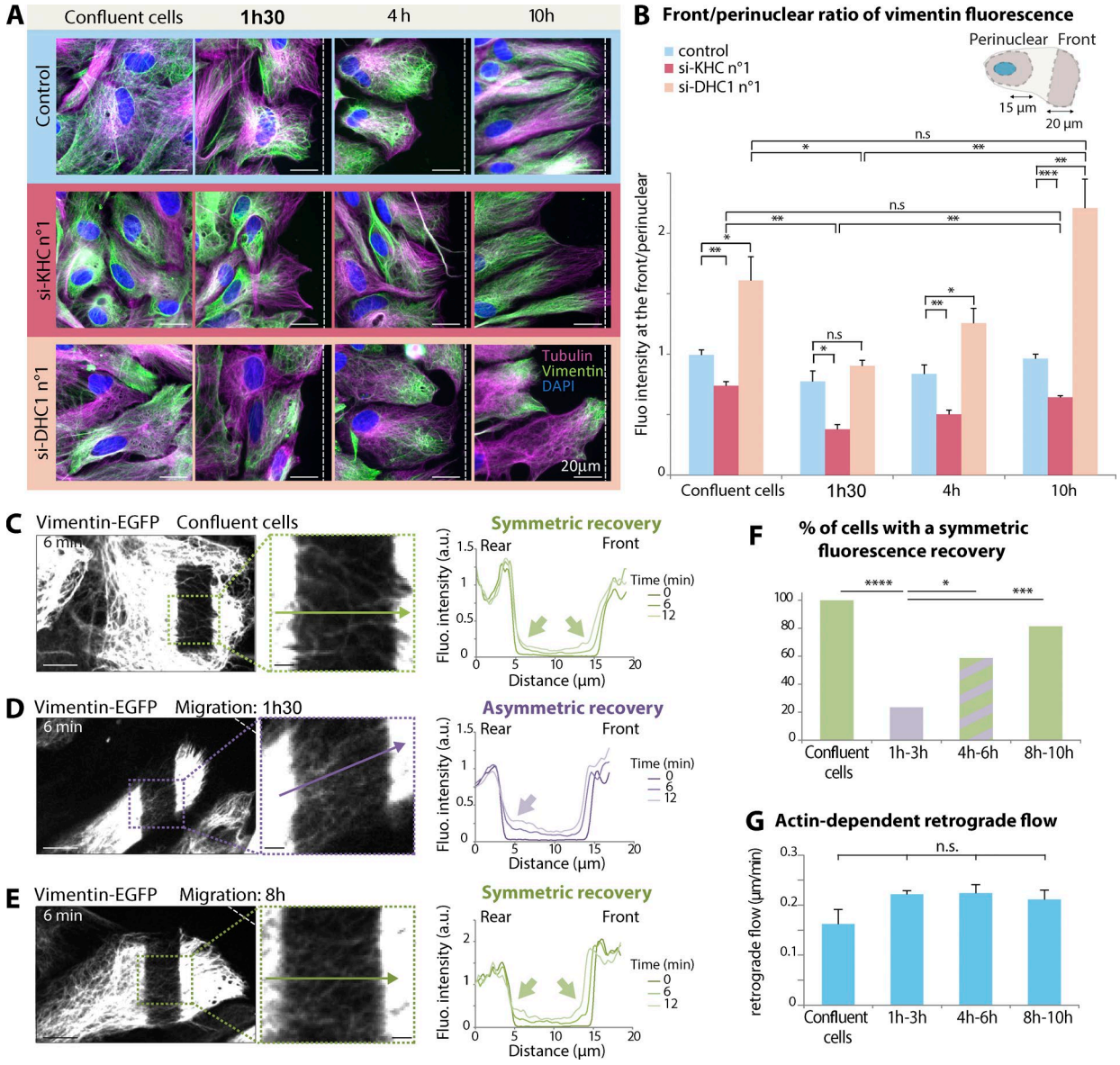

Figure 4. **Regulation of kinesin-1– and dynein-1– dependent transport drives the polarization of the IF network.** (A) Epifluorescence images of vimentin (green), tubulin (magenta), and DNA (blue) in migrating astrocytes (before wounding, 1 h 30 min, 4 h, and 10 h after wounding) 4 d after nucleofection with the indicated siRNAs (also see Fig. S3 A). Dashed lines indicate wound orientation. (B) Ratios between front and perinuclear vimentin fluorescence (Fluo) intensities before wounding (confluent cells) or at different times after wounding. Cells were nucleofected with the indicated siRNAs. The results are shown as means ± SEM of at least three independent experiments with ∼50 cells per time point, per condition, per repeat experiment; ∼1,800 cells were used in total. (C–E) Fluorescence images acquired 6 min after photobleaching during a FRAP experiments on vimentin-EGFP–expressing astrocytes in confluent cells (C) 1 h 30 min (D) and 8 h (E) after wounding (Video 7). Fluorescence intensity profiles along corresponding arrows show either a symmetric (C and E) or asymmetric (D) recovery of fluorescence. The higher-magnification images of regions indicated by a dotted line box are shown in corresponding dotted line boxes. Bars: (main images) 10 µm; (insets) 2 µm. Filled arrows point to the slopes observed in the fluorescence recovery profile, indicating a symmetric or asymmetric recovery of fluorescence. Note that in the case of asymmetry, the fluorescence recovery occurs only from the rear side of the photobleached area (shown by a single filled arrow). a.u., arbitrary units. (F) Percentages of cells displaying a symmetric fluorescence recovery in each condition (33–54 cells per condition in a minimum of three independent experiments). (G) Speed of the retrograde flow in each condition was extracted from the same data as in F. Means ± SEM of three independent experiments are shown. *, P < 0.05; **, P < 0.01; ***, P < 0.001; ****, P < 0.0001.

rate of 75%; Fig. S2 B). We estimated that labeled proteins represented between 4 and 34% of the total amount of vimentin in 90% of the cells, which did not affect the organization of the endogenous IF network (Fig. S2 C) nor cell motility. Between 1 and 8 h after wounding, the protrusion length and cell surface increased, whereas the mean intensity of vimentin staining decreased (Fig. S2 D), indicating that the IF network reorganized without any significant changes in the total amount of vimentin. We then assessed the role of microtubule-associated motors on IF distribution. In confluent astrocytes (nonmigrating and nonpolarized), kinesin-1 depletion by two different siRNAs specifically directed against the kinesin sequence (Fig. S3 A) led to an accumulation of the IF network around the nucleus (Fig. 4, A and B; and Fig. S2 E). In contrast, dynein-1 depletion by specific siRNAs (Fig. S3 A) induced vimentin accumulation at the cell periphery (Fig. 4, A and B; and Fig. S2 E). Control siRNA with a minimum number of mismatches did not have any effect (Figs. S2 E and S3 A).

During cell polarization (1 h 30 min and 4 h after wounding), the effect of motor depletion was different than in confluent nonpolarized cells. Although kinesin-1 depletion led to a significantly increased perinuclear accumulation of vimentin, dynein-1 depletion had a minimal impact on vimentin distribution (Fig. 4, A and B; small interfering kinesin heavy chain (KHC; siKHC) n°1 and small interfering dynein heavy chain 1 (DHC1; siDHC1) n°1, respectively). This decreased effect of dynein-1 depletion was transient and associated with the cell polarization. During steady-state directed migration (≥8 h after wounding), the effect of dynein depletion was recovered with an accumulation of vimentin at the cell periphery in dynein-depleted cells compared with control cells (Fig. 4, A and B). Similar results were obtained when looking at nestin or GFAP (Fig. S4, A and B).

Vimentin dynamics was assessed by photobleaching a rectangular region located at ∼15 µm to the wound edge, where the distribution of IFs was uniform. In nonmigrating confluent cells and steadily migrating polarized cells (8 h after wounding), a similar amount of IFs underwent anterograde transport from the "rear" edge of the photobleached region and retrograde transport from the "front" edge of the photobleached region. This resulted in a symmetric profile (see the Determination of the percentage of cells . . . section of Materials and methods) of fluorescence recovery (Fig. 4, C–F; and Video 7). In contrast, during polarization (1 h 30 min and 4 h after wounding), dynein-mediated retrograde transport was reduced, which resulted in an asymmetric profile of fluorescence recovery (Fig. 4, D and F; and Video 7). The profile of fluorescence recovery was asymmetric when the photobleaching was performed close to the cell front, but it remained symmetric in the nucleus proximity (Fig. S5 A), suggesting that the changes in IF dynamics are specifically controlled at the cell front. Western blot analysis also showed that the expression level of the molecular motors was not significantly affected by cell polarization (Fig. S5 B), indicating that only the activity of the molecular motors was modified upon cell wounding. In addition to the fast transport of filaments, a global retrograde flow of IFs similar to that described in astrocytoma cells (Fig. 2 B) was observed. This actin-driven retrograde flow did not significantly change during cell polarization (Fig. 4 G). FRAP experiments performed on astrocytes coexpressing vimentin-RFP/GFAP-EGFP and vimentin-RFP/nestin-EGFP confirmed that single filaments moving in the bleached region are composed of the three IF proteins (Fig. S4, C and D).

The directionality of vimentin transport is triggered by cell polarization

Cell wounding induces astrocyte polarization (cell orientation toward the wound) in parallel to the initiation of migration (protrusion formation and movement). Small GTPases of the Rho family have been shown to play a central role in these events (Etienne-Manneville, 2008; Zegers and Friedl, 2014; Ridley, 2015). Although both phenomena are induced by integrin engagement at the leading edge, cell polarization is controlled by a Cdc42-dependent, Rac1-independent signaling, whereas the initiation of cell motility and protrusion is controlled by Rac1 and not by Cdc42 (Etienne-Manneville and Hall, 2001). To distinguish between cell polarization and migration, astrocytes were immobilized on fibronectin-coated micropatterns surrounded by polyethylene glycol to prevent migration (Dupin et al., 2009, 2011). We used large (120-µm diameter) circular adhesive micropatterns that allowed the spreading of four to eight cells. After spreading, cells form intercellular contacts that trigger an intracellular polarization of the cells located at the periphery of the pattern (Dupin et al., 2009). Although the spreading area and the overall shape of the cells do not change, the nucleus moves away from the free edge, and the centrosome, microtubule network, and IFs localize in front of the nucleus in the direction of the free edge of the cells. In contrast, single cells plated on 50-µm diameter circular micropatterns remained nonpolarized. Inhibition of kinesin-1 resulted in vimentin perinuclear accumulation in isolated cells as well as in grouped cells (Fig. 5, A and B). In contrast, the role of dynein was strikingly different in isolated and in grouped cells. Although dynein depletion induced a strong accumulation of vimentin at the periphery of isolated astrocytes, it had a minor effect on vimentin distribution when a group of astrocytes were plated on large micropatterns (Fig. 5, A and B). FRAP experiments on grouped and individual cells plated on micropatterns confirmed that cell polarization, with limited morphological changes, led to a specific decrease in IF retrograde transport without affecting kinesin-1–dependent anterograde transport and actin-dependent retrograde flow (Fig. 5, C–F). These results indicate that the inhibition of IF anterograde transport observed after wounding of the astrocyte monolayer is triggered by structural cell polarization but does not require changes in cell morphology. Collectively, our observations indicate that the front–rear polarization of the IF network during the initiation of migration results from the regulation of kinesin- and dynein-mediated transports at the cell front but not from the actin-driven retrograde flow, which remains unchanged (Fig. 5 G).

We then tested whether Cdc42 was involved in the polarization of the IF network. Down-regulation of Cdc42 by two different specific siRNAs (Fig. S3 B) or Cdc42 specific inhibition by cell treatment with ML141 (Hong et al., 2013) prevented the reorientation of the IF network toward the wound edge (Fig. 6 A). In contrast, siRNA-mediated depletion of Rac1 (Fig. S3 B) prevented cell protrusion but did not affect the orientation of the IF network (Fig. 6 A). To determine whether Cdc42 plays a direct role in the control of dynein-mediated IF transport, we performed FRAP experiments on vimentin-EGFP–expressing cells. 1 h 30 min after wounding, the profile of fluorescence recovery at the front of control and Rac1-depleted cells was asymmetric (Fig. 6, B and C). In contrast, the fluorescence recovery profile remained symmetric in Cdc42-depleted cells, similar to that of nonpolarized cells (Fig. 6, B and C; and Video 8). In these conditions, the transport of vimentin filaments was observed in both anterograde and retrograde directions (Fig. 6 B and Video 8). Similar results were observed when astrocytes were treated with ML141, but not when it was treated with the Rac1 inhibitor NSC23766 (Fig. 6 C; Gao et al., 2004). These results indicate that the polarity protein Cdc42, which is activated at the cell wound edge during polarization (Etienne-Manneville and Hall, 2001; Osmani et al., 2006, 2010), locally inhibits dynein-mediated transport of IFs to promote the orientation of the IF network toward the wound. This transient inhibition of dynein-mediated transport was also triggered by cell treatment with bradykinin, a well-known activator of Cdc42 (Fig. 6, D and E; Kozma et al., 1995). Bradykinin's inhibitory effect on IF retrograde transport was abolished in Cdc42-depleted cells, confirming the role of Cdc42 in this phenomenon (Fig. 6 E). Interestingly, long-term exposure to bradykinin induced a Cdc42-dependent increase of the actin-dependent retrograde

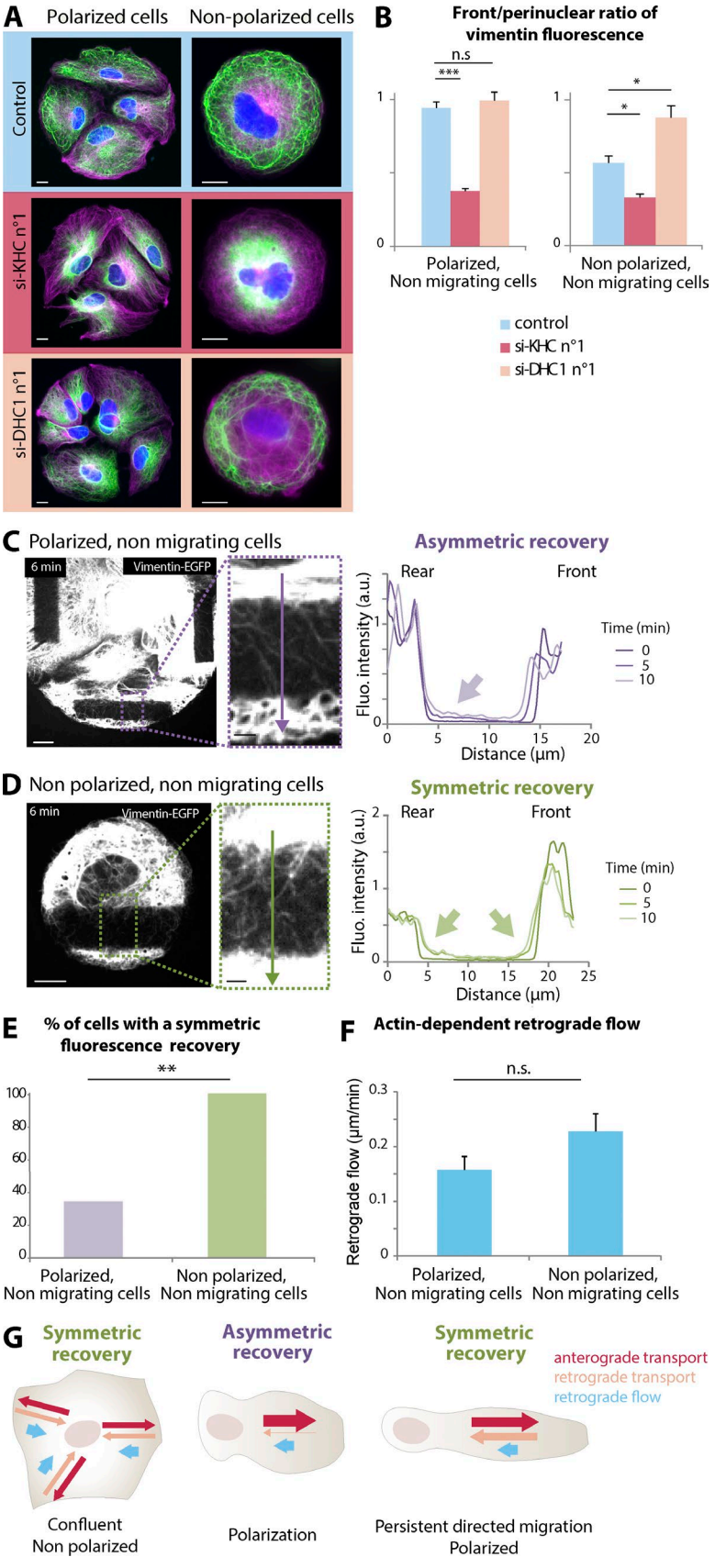

Figure 5. **Vimentin transport directionality is triggered by cell polarization.** (A) Merged images of vimentin (green), tubulin (magenta), and DNA (blue) of nonmigrating astrocytes plated on either 120-µm (polarized cells) or 50-µm disks (nonpolarized cells). Cells were nucleofected with the indicated siRNAs. Bars, 10 µm. (B) Ratio between peripheral and perinuclear vimentin intensity in each condition. Each experiment was repeated three times with ~50 cells per condition and per repeat. Error bars display the SEM for the three repeats. (C and D, left) Still fluorescence (Fluo.) images (6 min after photobleaching) of vimentin-EGFP–expressing astrocytes: five to eight cells were plated on 120-µm diameter micropatterns (C), and single cells were plated on a 50-µm diameter circular micropatterns (D). Bars: (main images) 10 µm; (insets) 2 µm. (Right) Fluorescence intensity profiles along the corresponding arrows showing the fluorescence recovery at different time points after photobleaching. Filled arrows point to the slopes observed in the fluorescence recovery profile, indicating a symmetric or asymmetric recovery of fluorescence. Note that in the case of asymmetry, the fluorescence recovery occurs only from the rear side of the photobleached area (shown by a single filled arrow). a.u., arbitrary units. (E) Percentages of cells displaying a symmetric fluorescence recovery (32 polarized nonmigrating cells and 15 nonpolarized nonmigrating cells out of three and five independent experiments, respectively). (F) Quantification of the vimentin retrograde flow. Error bars display SEM for the three repeats with 32 and 15 cells per condition, respectively. *, $P < 0.05$; **, $P < 0.01$; ***, $P < 0.001$. (G) Schematics of IF dynamics during cell polarization and migration. Arrows correspond with colored labels on the right.

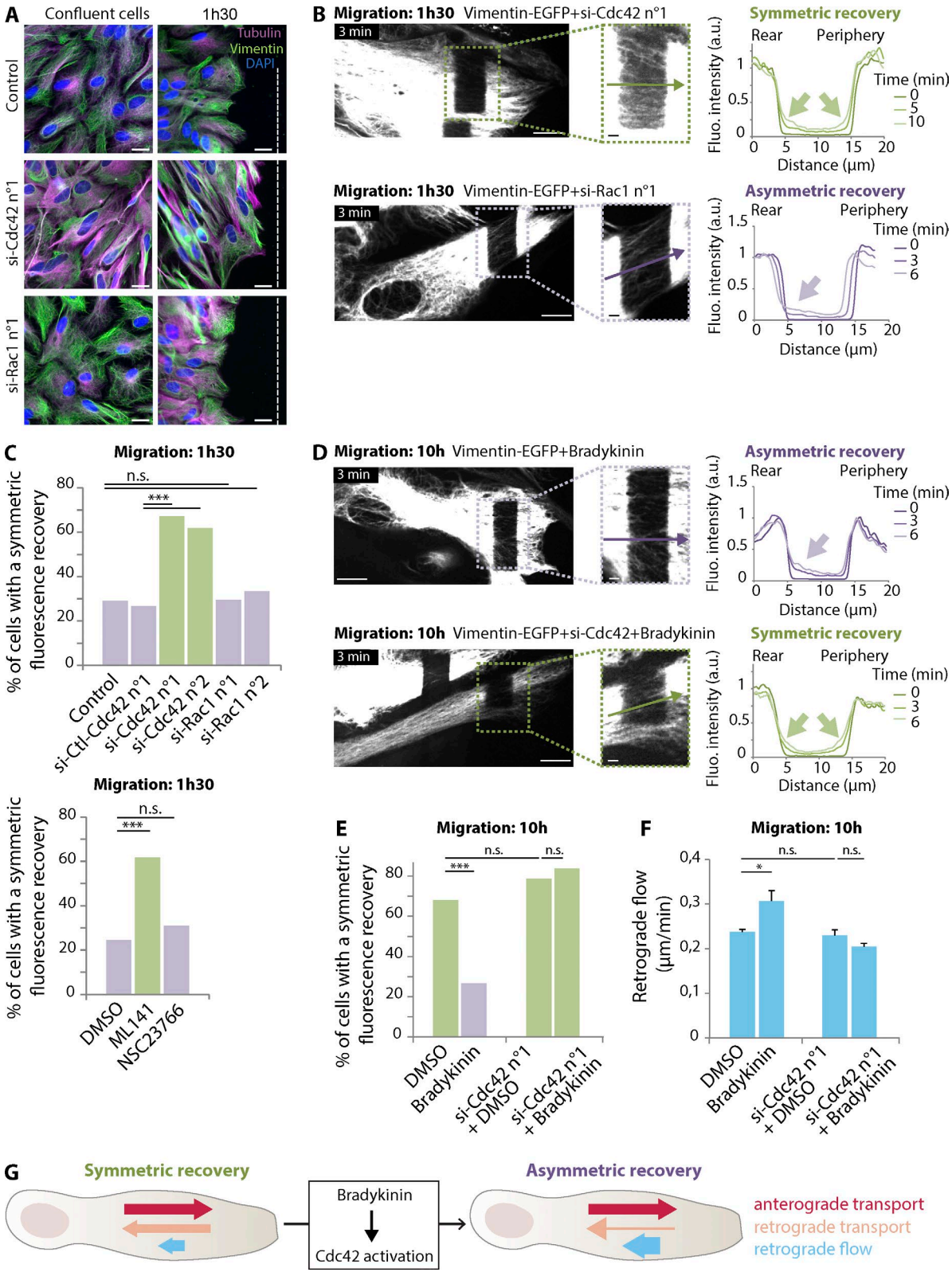

Figure 6. **Vimentin dynamics is regulated by Cdc42 during cell polarization.** (A) Merged images of vimentin (green), tubulin (magenta), and DNA (blue) of astrocytes before or 1 h 30 min after wounding. Cells were nucleofected with indicated siRNAs (also see Fig. S3 B). The orientation of the wound is shown with dashed lines. Bars, 20 µm. (B, left) Still fluorescence (Fluo.) images 3 min after photobleaching from a FRAP experiment performed with vimentin-EGFP–expressing astrocytes 1 h 30 min after wounding. Wounding was done 4 d after cell nucleofection with the indicated siRNAs (see Video 8 for small interfering Cdc42). The contrast was increased in the zoom of Cdc42-depleted cell to better show the emergence of vimentin filaments in the photobleached region. (Right) fluorescence intensity profiles showing the fluorescence recovery at different time points after photobleaching. (C) Percentages of cells displaying a symmetric FRAP 1 h 30 min after wounding. Cells were nucleofected with the indicated siRNA or treated with DMSO, ML141 (inhibitor of Cdc42; 10 µM added 1 h before wounding), and NSC23761 (inhibitor of Rac1; 50 µM added 1 h before wounding; 44–66 cells per condition with a minimum

flow of IFs (Fig. 6 F), which might explain the collapse of IF network observed in other cell types (Meriane et al., 2000).

aPKC mediates Cdc42's effect on IF transport independently of its role in centrosome reorientation

The small GTPase Cdc42 acts as a molecular switch that activates a wide variety of effector proteins (Etienne-Manneville and Hall, 2002). Among these effectors, the polarity complex Par6–aPKC has been shown to play a key role in Cdc42-mediated cell polarization (Etienne-Manneville and Hall, 2003). Inhibition of aPKC using two different specific siRNAs (Fig. S3 C) or cell treatment with the PKCζ pseudosubstrate abolished the inhibition of IF retrograde transport during cell polarization 1 h 30 min after wounding, leading to a symmetric fluorescence recovery (Fig. 7, A–C; and Video 9). In contrast, depletion of another Cdc42 effector, the Neural–Wiskott Aldrich Syndrome protein (N-WASp; Western blot in Fig. S3 C), or cell treatment with the N-WASp inhibitor wiskostatin (Peterson et al., 2004) did not alter the fluorescence recovery profile 1 h 30 min after wounding (Fig. 7, A–C). Furthermore, the asymmetry of IF transport in Cdc42-depleted cells was rescued by overexpressing PKCζ-GFP (Fig. 7, D–F; and Video 10) suggesting that aPKCζ is the major effector of Cdc42 in the control dynein-mediated IF transport.

We have previously shown that aPKC mediates Cdc42-dependent centrosome positioning by inducing the interaction between Dlg1 and microtubule plus end–associated adenomatous polyposis coli to promote the cortical anchoring of microtubules at the cell front (Etienne-Manneville et al., 2005; Manneville et al., 2010). To determine whether aPKC-mediated regulation of IF transport was a consequence of its function in the regulation of microtubule anchoring at the leading edge, we analyzed IF dynamics by FRAP in Dlg1-depleted cells (Fig. 7, A–C). Dlg1 depletion had no effect on the directionality of the IF transport during cell polarization, whereas it prevented correct centrosome orientation (Etienne-Manneville et al., 2005; Manneville et al., 2010). Collectively, these results indicate that the Par6–aPKC complex acts downstream of Cdc42 to control dynein-mediated transport of IF and promote the polarization of the IF network independently of its impact on microtubule reorganization (Fig. 7 F).

Discussion

We show here that the organization of the IF network involves a combination of active processes: kinesin-1– and dynein-1–mediated transport along microtubules and actin-dependent retrograde flow. FRAP and local photoconversion experiments performed in motile cells allowed us to differentiate the three modes of motion. At steady state, a balance between these three modes of transport enables a dynamic turnover of the network. During cell polarization, the reorientation of the IF network toward the leading edge results from the inhibition of dynein-mediated transport at the cell front, which contributes to maintain a uniform distribution of IFs throughout the cytoplasm (Fig. 5 G).

In a 2D migration assay of glial cells, we observed that the dynamics and the organization of the type III IF network mainly involves the movement of preexisting mature filaments with a wide range of lengths (micrometers to tens of micrometers) throughout the cytoplasm. Superresolution images of single filaments showed that vimentin, GFAP, and nestin, which are coexpressed in astrocytes and astrocytoma cells, can be found together in single IFs. We observed subdomains in which only one of the proteins was present. Single filaments could be formed by the annealing or exchange of these short subdomains (Hookway et al., 2015) or by direct copolymerization of two or three of the IF proteins, as previously observed in vitro (Steinert et al., 1999a,b; Herrmann and Aebi, 2000; Wickert et al., 2005).

The transport of IF precursors or particles is much less frequent compared with what was observed for vimentin polymers (Hookway et al., 2015; Robert et al., 2016) and for keratins in epithelial cells (Kölsch et al., 2009, 2010). Although we did not observe severing and annealing events in our FRAP and photoconversion videos, we cannot rule out that they occasionally occur (Hookway et al., 2015). Interestingly, cell morphology and tension strongly impact on the ratio between polymerized and nonpolymerized forms of vimentin (Murray et al., 2014) and may affect polymerization and annealing. It will be interesting to study how IF dynamics are modified in cells plated on a soft substrate or in cells migrating in a 3D environment, which are known to alter cellular tension and morphology.

Polymerization/depolymerization events and subunit exchange were negligible within the time scale of our studies, indicating that the IF network dynamics mainly involved microtubule-dependent transport. We observed bidirectional transport, which could result from a "tug of war" between kinesin and dynein motors attached to the same filaments (Hancock, 2014). Although seemingly inefficient, such transport mechanisms could facilitate the transport of long cargoes (sometimes >10 µm long) around obstacles located along the microtubules (Hancock, 2014).

Cell migration requires the polarized reorganization of the cytoskeleton. Recruitment of vimentin at the cell front contributes to focal adhesion maturation (Bhattacharya et al., 2009; Burgstaller et al., 2010). Vimentin uncoupling from focal adhesions impairs directed cell migration (Gregor et al., 2014). Vimentin IFs can also promote cell spreading independently of their role in the regulation of focal adhesions (Lynch et al., 2013). Moreover, the IF network participates in the polarized organization of the microtubule network (Dupin et al., 2011; Shabbir et al., 2014), hinting at a positive feedback between the

of three independent experiments). (D, left) Still fluorescence images acquired 3 min after photobleaching of vimentin-EGFP–expressing astrocytes 10 h after wounding. Control or Cdc42-depleted cells were left treated with DMSO or with bradykinin (10 µM) 1 h before the FRAP experiment. (Right) Fluorescence intensity profiles along the corresponding arrows showing the fluorescence recovery at different time points after photobleaching. Filled arrows point to the slopes observed in the fluorescence recovery profile, indicating a symmetric or asymmetric recovery of fluorescence. Note that in the case of asymmetry, the fluorescence recovery occurs only from the rear side of the photobleached area (shown by a single filled arrow). (B and D) Bars: (main images) 10 µm; (insets) 2 µm. a.u., arbitrary units. (E) Percentages of cells displaying a symmetric profile of FRAP after 10 h of migration. Control or Cdc42-depleted cells were left treated with DMSO or bradykinin (10 µM; 1 h; 37–60 cells per condition with a minimum of three independent experiments). (F) Quantification of the vimentin retrograde flow in the experiments described in E. Error bars display SEM for the three repeats. *, $P < 0.05$; ***, $P < 0.001$. (G) Schematics representing the mechanisms involved in IF dynamics after Cdc42 activation by Bradykinin treatment. Arrows correspond with colored labels on the right.

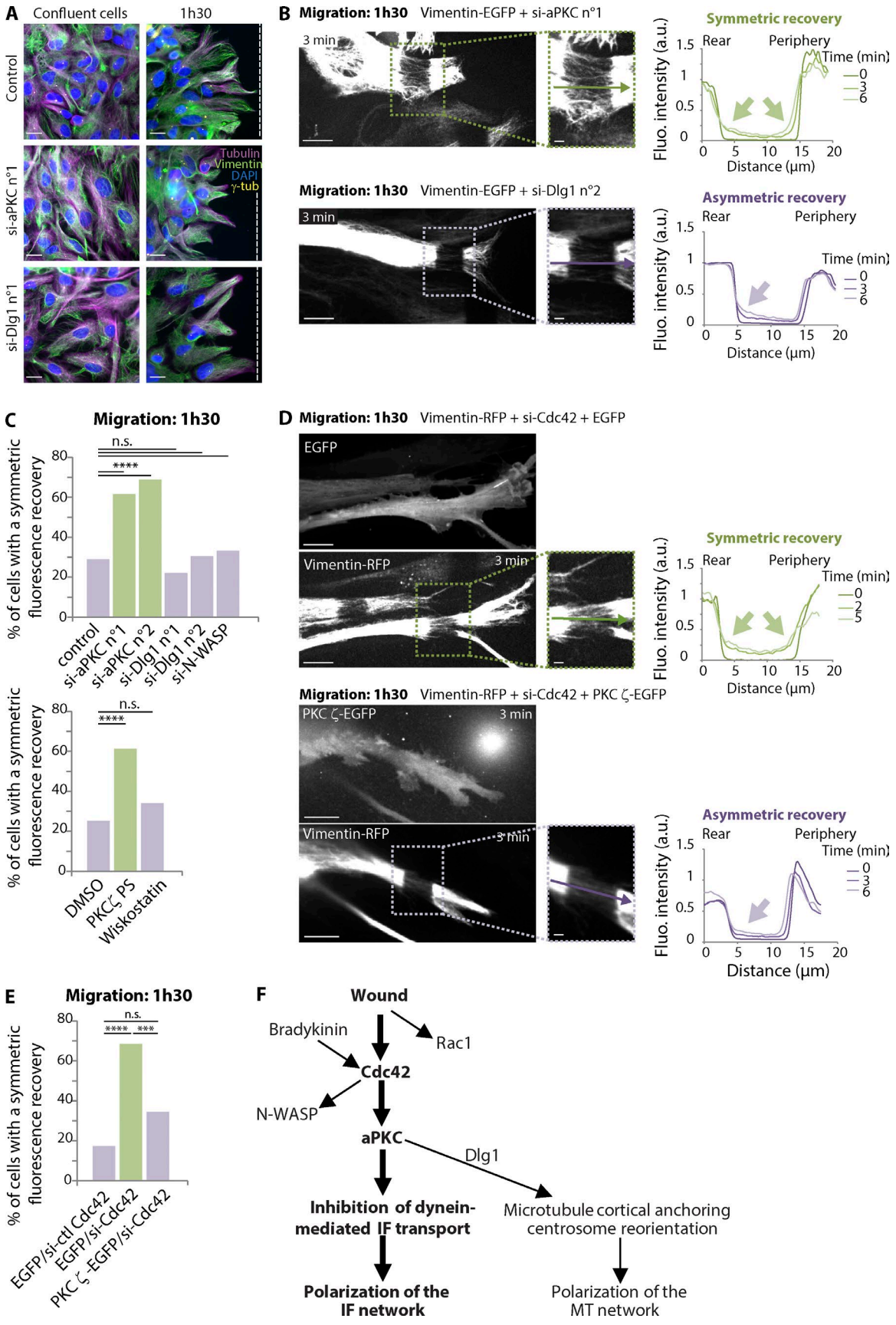

Figure 7. **Vimentin dynamics are regulated by aPKC during cell polarization.** (A) Merged images of vimentin (green), tubulin (magenta), γ-tubulin (γ-tub; yellow), and DNA (blue) of astrocytes 4 d after transfection with indicated siRNAs (also see Fig. S3 C). Dashed lines indicate wound orientation. Bars, 20 µm. (B, left) Still fluorescence (Fluo.) images 3 min after photobleaching of vimentin-EGFP–expressing astrocytes 1 h 30 min after wounding. Cells were

two cytoskeletal networks (Gan et al., 2016). The tight physical interaction between IFs and microtubules (Fig. 3, D–F) is likely to play a key role in this cytoskeletal interplay.

Astrocyte polarization includes the reorientation of the microtubule organizing center, the microtubule network, the Golgi apparatus, membrane trafficking, and the extension of IF network along the polarity axis toward the leading edge (Etienne-Manneville, 2006; Peglion et al., 2014). In this study, we observed that during cell polarization, microtubule-dependent IF transport was biased toward the cell front, whereas the actin-dependent retrograde flow remained unchanged. Dynein inhibition was specifically required for the polarized reorganization of IFs, even in the absence of major cell shape changes and cell migration on micropatterns. Nevertheless, we cannot exclude that the inhibition of dynein-dependent retrograde transport directly contributed to the formation of the long astrocytic processes that formed during the first hours of direction migration. Once cells reached a steady state of migration with a stable elongated shape, dynein-mediated transport was reestablished, whereas kinesin-mediated transport remained high and may have contributed to keeping a constant level of filaments at the cell front.

The small GTPase Cdc42 is a central player in the control of cell polarity (Etienne-Manneville, 2004). During front–rear polarization of migrating cells, it participates in the formation of actin structures of the cell front and plays an essential role in the polarization of the microtubule network. We show here that Cdc42 is also crucial for the polarized rearrangement of IFs, uncovering a central role of Cdc42 in the coordination of the three filamentous networks (Meriane et al., 2000; Chan et al., 2002; Etienne-Manneville, 2004). The function of Cdc42 in cell polarity frequently involves its effector complex, Par6–aPKC (Etienne-Manneville and Hall, 2003). aPKC controls centrosome positioning, microtubule network polarization, and directed persistent migration. aPKC also acts downstream of Cdc42 to regulate IF transport during cell polarization. The impact of Cdc42 and aPKC on the organization of the IF network does not only result from the global alteration of the other cytoskeletal elements, but specifically affects microtubule-driven IF retrograde transport. Whether Cdc42-mediated signaling controls dynein function and/or dynein association with IFs remains to be clarified. However, we could not detect any major inhibition of dynein-mediated vesicular transport, suggesting that Cdc42 may specifically affect IF transport. Cdc42-mediated signaling can affect dynein localization at the leading edge (Etienne-Manneville and Hall, 2001; Palazzo et al., 2001; Dujardin et al., 2003; Manneville et al., 2010) to anchor microtubules and promote centrosome reorientation (Manneville et al., 2010). The recruitment of dynein along anchored microtubules requires Dlg1, which does not affect IF transport strongly, suggesting that the regulation of dynein-mediated IF transport occurs independently of the regulation of microtubule anchoring and centrosome reorientation.

Astrocytes are major glial cells of the central nervous system that migrate collectively during development (Chu et al., 2001; Fruttiger, 2002; Gnanaguru et al., 2013). In the normal adult brain, these cells are immobile, but their migration can be induced in response to inflammatory situations associated with physical trauma (Faber-Elman et al., 1996; Sofroniew, 2009). Astrocytes are a particularly interesting model, as they express a well-characterized subset of the IF proteins vimentin, GFAP, nestin, and possibly synemin (Sultana et al., 2000). GFAP is a specific marker of differentiated astrocytes, whereas nestin tends to characterize less differentiated cells. Moreover, GFAP overexpression is a well-known marker of reactive astrocytes. We did not detect any differences in the behavior of vimentin, GFAP, and nestin, as expected, because the three proteins appear to copolymerize and form IFs of mixed composition. One interesting possibility is that changes in IF composition could affect their interaction with the various elements that control their dynamics (including microtubule-associated motors) and modify the impact of regulatory pathways. Further studies will be necessary to elucidate the links between IF proteins and molecular motors, whether they are direct or indirect and specific to certain IF proteins. Disease-associated mutations of IF proteins might affect their association with molecular motors and thereby lead to an altered organization of the IF network, contributing to the disease. Differences in IF composition between normal astrocytes and astrocytoma cells may also be responsible for the difference in IF dynamics observed in these cells. More generally, dramatic changes in IF composition have been observed in cancer cells (Leduc and Etienne-Manneville, 2015) and may be involved in the alteration of cell polarity and migration. A recent study showed that astrocytoma grade IV (glioblastoma multiforme), which is the most common and most malignant tumor of the central nervous system and is currently incurable, displays three subtypes with unique expression profiles of IF proteins (Skalli et al., 2013). GFAP levels in patient blood could be used as a biomarker for the diagnosis of invasive glioblastomas (Jung and Jung, 2007; Ilhan-Mutlu et al., 2013), and expression levels of GFAP are correlated with the invasive capacities of glioblastomas (Maslehaty et al., 2011). It will be interesting to characterize in more detail how the IF composition impacts on the IF network dynamics and reorganization and also on the cell's ability to migrate in the brain tissue.

Materials and methods

Antibodies, constructs, siRNA, and reagents

We used the following antibodies: vimentin from Sigma-Aldrich (V6630) and Santa Cruz Biotechnology, Inc. (sc-7557R), GFAP from Dako (z0334) and Santa Cruz Biotechnology, Inc. (sc-6170), α-tubulin from AbD Serotec/Bio-Rad Laboratories (MCA77G), kinesin-1 SUK4 from Abcam (ab280060), dynein intermediate chain from Covance

nucleofected with the indicated siRNAs (see Video 9 for small interfering aPKC [si-aPKC]). (Right) Line profiles showing the FRAP. (C and E) Percentages of cells displaying a symmetric profile of FRAP 1 h 30 min after wounding. Cells were nucleofected with the indicated siRNA or constructs and then were left untreated or treated with DMSO, PKCζ pseudosubstrate (PS; inhibitor of PKCζ; 10 µM was added 1 h before wounding), and wiskostatin (inhibitor of N-WASp; 2 µM was added 1 h after wounding). Statistics include 36–74 cells per condition from a minimum of three independent experiments. (D, left) Still fluorescence images acquired 3 min after photobleaching of Cdc42-depleted astrocytes expressing vimentin-RFP and either EGFP or PKCζ-EGFP (Video 10) 1 h 30 min after wounding. (Right) Line profiles showing the FRAP. Filled arrows point to the slopes observed in the fluorescence recovery profile, indicating a symmetric or asymmetric recovery of fluorescence. Note that in the case of asymmetry, the fluorescence recovery occurs only from the rear side of the photobleached area (shown by a single filled arrow). Bars: (main images) 10 µm; (insets) 2 µm. a.u., arbitrary units. (F) Schematic diagram showing the "front" polarity signaling triggering the polarized rearrangements of IFs and microtubules during astrocyte polarization. MT, microtubule.

(MMS-400P), Cdc42 from BD (610929), Rac1 from EMD Millipore (05-389), aPKC from Santa Cruz Biotechnology, Inc. (sc-17781) that recognizes both isoforms PKCζ and PKCι, N-WASp from Abcam (ab187527), Dlg1 from BD (610875), actin from Sigma-Aldrich (A2228), and GAPDH (MAB374) from EMD Millipore.

Secondary antibodies were purchased from Jackson ImmunoResearch Laboratories, Inc.

The following plasmids were gifts: pEGFP-N3-vimentin and pEGFP-N3-GFAP from D. Pham-Dinh (Université Pierre et Marie Curie, Paris, France), Lifeact-mCherry from M. Piel (Institut Curie, Paris, France), mCherry-tubulin from A. Echard (Institut Pasteur, Paris, France), and PKCζEGFP from C. Rossé (Institut Curie, Paris, France; Rossé et al., 2014). Mouse vimentin was subcloned in pDendra2-N1 with EcoRI and SalI. pNestin-EGFP was purchased from Addgene (38777).

We used the following rat siRNAs: KHC n°1, 5′-AUGCAUCUC GAGACCGCAA-3′; KHC n°2, 5′-UGAAUUGCUUAGUGAUGAA-3′; control KHC n°1 (si-ctl KHC n°1) with four mismatches, 5′-UUG CUUCUCCUGACCGCAA-3′; DHC1 n°1, 5′-UGCCAAGUUUAA CUACGGC-3′; DHC1 n°2, 5′-GCUCAACCCCAGGAAAUC-3′ (Manneville et al., 2010); control DHC1 n°1 (si-ctl DHC1 n°1) with four mismatches, 5′-UACCGUGUUUACCUACGGC-3′; Cdc42 n°1, 5′-AGAUGGUGCUGUUGGUAAA-3′; Cdc42 n°2, 5′-GAAUGU GUUUGAUGAAGCA-3′ (Osmani et al., 2010); control Cdc42 n°1 with four mismatches, 5′-CGAUGAUGCUGCUGGUCAA-3′; Rac1 n°1, 5′-AUGUCCGUGCAAAGUGGUA-3′; Rac1 n°2, 5′-CCUGCC UGCUCAUCAGUUA-3′; Dlg1 n°1, 5′-CACAGACAGCUUGGA GACA-3′; Dlg1 n°2, 5′-UUCGGAGAUAUUCUCCAUG-3′ (Etienne-Manneville et al., 2005); aPKC n°1 (PKCζ + PKCι), 5′-CUUAAG CCUGUCAUCGAUG-3′ + 5′-UACCAGAGCGUCCUGGAAU-3′; aPKC n°2 (PKCζ + PKCι), 5′-ACAUUAAGCUGACGGACUA-3′ + 5′-GAGAGGAGUUACGCCAAA-3′; and N-WASp, 5′-AAGACG AGAUGCUCCAAAU-3′. Human siRNAs were: KHC, 5′-AUGCAU CUCGUGAUCGCAA-3′; and DHC1, 5′-UGCCAAAUUUAACUA UGGC-3′; and displayed two mismatches with rat siKHC n°1 and rat siDHC1 n°1 and produced partial knockdown of the corresponding proteins (Fig. S3 A).

Cell culture

Primary rat astrocytes were prepared as previously described (Etienne-Manneville, 2006) according to the guidelines approved by the French Ministry of Agriculture and following European standards. For scratch-induced migration assays, cells were seeded on poly-L-ornithine–precoated coverslips for immunofluorescence or 35-mm glass-bottomed culture dishes (MatTek Corporation) for videomicroscopy. Cells were grown to confluence in DMEM with 1 g/l glucose and supplemented with 10% FBS (Invitrogen), 1% penicillin–streptomycin (Thermo Fisher Scientific), and 1% amphotericin B (Thermo Fisher Scientific). On the day of the experiment, cells were scratched with a blunt-ended microinjection needle, creating a 300-µm-wide wound to trigger cell migration. U373 astrocytoma cells were grown to confluence in DMEM-F12 (Invitrogen) supplemented with 10% FBS (Invitrogen), 1% penicillin–streptomycin, and 1% nonessential amino acids (Thermo Fisher Scientific).

Cell transfection

Starting from a 10-cm Petri dish, cells grown to confluence were trypsinized and electroporated with a nucleofector machine (Lonza). We used 5 µg of DNA or 1 nmol of siRNA for astrocytes and 2.5 µg of DNA for U373 astrocytoma cells. Medium was changed 1 d after transfection and 1 d before the experiments. Optimal protein depletion was observed 4 d after nucleofection.

Drug and hormonal treatments

Drugs were added 1 h before wounding the monolayer except for the drugs that destabilize the cytoskeleton, which were added 1 h after wounding to allow protrusion formation and initiation of cell migration. Blebbistatin was used at 2 µM, latrunculin A at 20 µM, nocodazole at 10 µM, ML141 (Cdc42 inhibitor) at 10 µM, NSC23766 (Rac1 inhibitor) at 50 µM, wiskostatin (N-WASp inhibitor) at 2 µM, and PKCζ pseudosubstrate at 10 µM. Bradykinin was added 9 h after wounding and 1 h before FRAP experiments at a final concentration of 10 µM. Nocodazole, latrunculin A, and ML141 were purchased from EMD Millipore, blebbistatin from Sigma-Aldrich, NSC23766 from Tocris Bioscience, and wiskostatin, PKCζ pseudosubstrate, and bradykinin were from Enzo Life Sciences.

Western blotting

Cell lysates were obtained using Laemmli buffer containing 60 mM Tris-HCl, pH 6.8, 10% glycerol, 2% SDS, and 50 mM DTT. Proteins were analyzed by 10% SDS-PAGE and transferred overnight at 4°C on nitrocellulose membranes. Antibodies were diluted in PBS with 0.2% Tween-20 and 4% milk or in TBS with 0.2% Tween-20 and 4% milk and applied at room temperature for 2 h. Washes were conducted with TBS with 0.2% Tween-20. Proteins were detected with the appropriate HRP-conjugated secondary antibodies detected by an ECL chemiluminescent substrate (Thermo Fisher Scientific).

Immunofluorescence

Cells were fixed in cold methanol for 5 min and blocked with 3% BSA in PBS for 1 h. Cells were then incubated for 1 h with primary antibodies, washed three times in PBS, and incubated another hour with secondary antibodies. Finally, coverslips were washed and mounted in ProLong Gold with DAPI (Thermo Fisher Scientific). Epifluorescence images were obtained on a microscope (DM6000; Leica Biosystems) equipped with 40×, 1.25 NA, and 63×, 1.4 NA, objective lenses and were recorded on a charge-coupled device camera using Leica Biosystems software. To compare fluorescence intensities from staining of different conditions, acquisition parameters (intensity, gain, and exposure time) were kept constant.

STORM

Cells were fixed in cold methanol for 5 min and immunostained with anti-tubulin (rat) and anti-vimentin (mouse). The secondary antibodies anti–rat TRITC and anti–mouse Alexa Fluor 647 were used at dilutions of 1:1,000. STORM images were acquired with an Elyra microscope (ZEISS) in a total internal reflection fluorescence mode using a buffer composed of 50 mM Tris-HCl, pH 8, 10 mM NaCl, 10% glucose, 0.5 mg/ml glucose oxidase, 40 mg/ml catalase, and 143 mM β-mercaptoethanol. 20,000 frames were acquired with 50-ms exposure times, and drift was automatically corrected by Zen software (ZEISS) using an autocorrelation analysis.

Kymograph analysis

Kymographs were calculated using an ImageJ plugin (National Institutes of Health). On each kymograph, three lines were plotted at the cell front to measure the velocity of the retrograde flow. The three values were averaged to calculate the retrograde flow within the cell reference frame.

Live-cell imaging

Nucleofected primary astrocytes or astrocytoma U373 cells were seeded on 35-mm glass-bottomed dishes and grown to confluence for 4 d. On the day before wounding, the medium was changed to a phenol red–free DMEM supplemented with 10% serum. The monolayer was wounded and cells were monitored 4 h later, allowing them to grow a

polarized protrusion. Videos were acquired on a spinning-disk confocal microscope (PerkinElmer) equipped with an electron-multiplying charge-coupled device camera and either a 63×, 1.4 NA objective or a 100×, 1.4 NA objective.

Calculation of the front/rear ratio of vimentin

For each cell, the mean fluorescence intensity was calculated at the cell periphery in a 20-µm-wide region and around the nucleus in a 15-µm-wide region (Fig. 4 B) using the image analysis software Fiji (ImageJ; Schindelin et al., 2012). The ratio between the two mean intensities gave an estimation of how uniform the vimentin was distributed inside the cell.

Determination of the percentage of cells with symmetric recovery after photobleaching

We considered the FRAP to be asymmetric when the fluorescence intensity profile showed a gradient only on the rear edge of the bleached region. Fluorescence intensity profiles showing fluorescence intensity gradients at both edges of the bleached region were considered to be symmetric, even though the gradients had different values. Note that the classification of cells with and without symmetric recovery is independent of the actin-driven global retrograde flow, which was observed by a shift of bleached region edges toward the cell rear.

Micropatterns

The micropatterning technique was used to impose reproducible cell shapes and decipher cell morphogenesis and functions (Théry, 2010). We have previously used astrocytes plated on micropatterns to study cell polarization (Dupin et al., 2015). In brief, primary rat astrocytes were plated onto glass-bottomed tissue culture dishes coated with fibronectin after deep UV micropatterning of the surrounding polyethylene glycol. We used two different shapes: 120-µm disks where groups of four to eight cells were plated and 50-µm diameter disks where only single cells were allowed to spread. In the case of the 120-µm disks, cells localized at the edge of the patterns formed anisotropic cellular interactions, which lead to cell polarization toward the periphery of the pattern (Dupin et al., 2009). Cells underwent limited morphological shape changes during the polarization process. They could not adhere outside of the pattern and thus did not form protrusions. Cell polarization occurred during the first 7 h of spreading but was not observed on the 50-µm disk micropatterns.

Colocalization analysis

Quantification of vimentin–nestin and vimentin–GFAP colocalization was performed on epifluorescence images of astrocytes fixed and immunostained with vimentin, GFAP, and nestin using the "Colocalization Threshold" plugin of ImageJ. We calculated for 26 cells the percent intensity above threshold colocalized between the two channels, which was different for each channel, and obtained values above 98% for each channel, condition, and cell. We also calculated the thresholded Mander's split colocalization coefficients (0 indicates no colocalization, 1 indicates perfect colocalization) and obtained values above 0.98 for each cell, channel, and condition (vimentin–nestin and vimentin–GFAP). The threshold values for each channel were determined iteratively using the Costes method. For each cell and condition (vimentin–nestin and vimentin–GFAP), we used the "Colocalization Test" plugin to verify that none of the randomized images calculated by the plugin gave better correlation between the two channels.

Statistics

The calculation of the front/rear ratio of vimentin (Figs. 4 B and S2 E) and the data presented in Fig. S2 D were obtained with ∼50 cells per time point, per condition, and per experiment, with a minimum of three repeats per condition. All data are presented as means ± SEM of three independent experiments and are compared with unpaired Student's *t* tests. Statistical differences were determined using Student's *t* tests. A p-value below 0.05 was considered to be statistically significant. *, $P < 0.05$; **, $P < 0.01$; ***, $P < 0.001$; ****, $P < 0.0001$.

The calculation of the p-value for the percentage of cells (Figs. 4 F, 5 E, 6, C and E; and 7, C and E) with symmetric fluorescence recovery was obtained with a χ^2 test for contingency. We analyzed 32–68 cells per condition obtained from three independent repeats in FRAP experiments on migrating astrocytes and astrocytes plated on large micropatterns, and we also analyzed 15 single cells out of five independent experiments for the astrocytes plated on the small micropatterns.

Statistical analysis was performed using Prism (5.0; GraphPad Software).

Online supplemental material

Fig. S1 shows how tubulin and vimentin dynamics are different when probed by FRAP. Fig. S2 shows the retrograde flow of vimentin dragged by actin filaments, how vimentin-GFP is inserted in the global IF network, and how vimentin quantity is not modified during cell migration. Fig. S3 shows the knockdown of the proteins analyzed in this study after Western blot analysis. Fig. S4 shows that GFAP and nestin behave similarly to vimentin in astrocytes. Fig. S5 shows that vimentin retrograde transport is inhibited only in the protrusion of polarizing astrocytes and not in the perinuclear region and that the quantity of molecular motors is not modified during cell migration. Videos 1 and 6 show the migration of an astrocytoma and astrocytes expressing vimentin-GFP. Video 2 shows a FRAP experiment on an astrocytoma expressing both vimentin-EGFP and tubulin-mCherry, and Video 5 shows their coordinated dynamics. Video 3 shows the dynamics of vimentin-Dendra2 after photoconversion. Video 4 shows the coordinated dynamics of vimentin-EGFP and Lifeact-mCherry. Video 7 shows the difference of vimentin dynamics in nonpolarized nonmigrating, polarizing, and polarized migrating astrocytes when probed by FRAP. Videos 8, 9, and 10 show that Cdc42 and aPKC depletion leads to the absence of dynein-mediated transport inhibition in polarizing migrating astrocytes (1 h 30 min after wounding).

Acknowledgments

We thank Mathieu Piel, Arnaud Echard, Danielle Pham-Dinh, and Carine Rossé for reagents and equipment, Jean-Baptiste Manneville and the Etienne-Manneville group for continuous support and careful reading of the manuscript, and Stéphanie Portet and Andrea Parmeggiani and his group for stimulating discussions. We gratefully acknowledge Jean-Yves Tinevez, Audrey Salles, and the Imagopole of Institut Pasteur (Paris, France) as well as the France–BioImaging infrastructure network supported by the French National Research Agency (ANR-10–INSB–04; Investments for the Future), and the Région Ile-de-France (program Domaine d'Intérêt Majeur-Malinf) for the use of the Elyra microscope.

This work was supported by the Institut National du Cancer, the Association pour la Recherche Contre le Cancer, the Ligue Contre le Cancer, the Centre National de la Recherche Scientifique, the Institut Pasteur, and the French National Research Agency (ANR-16-CE13-0019).

The authors declare no competing financial interests.

Author contributions: C. Leduc performed all the experiments and analysis. C. Leduc and S. Etienne-Manneville conceived the project, interpreted the data, and wrote the manuscript.

Submitted: 13 July 2016
Revised: 16 January 2017
Accepted: 3 March 2017

References

Bhattacharya, R., A.M. Gonzalez, P.J. Debiase, H.E. Trejo, R.D. Goldman, F.W. Flitney, and J.C. Jones. 2009. Recruitment of vimentin to the cell surface by β3 integrin and plectin mediates adhesion strength. *J. Cell Sci.* 122:1390–1400. http://dx.doi.org/10.1242/jcs.043042

Burgstaller, G., M. Gregor, L. Winter, and G. Wiche. 2010. Keeping the vimentin network under control: Cell–matrix adhesion-associated plectin 1f affects cell shape and polarity of fibroblasts. *Mol. Biol. Cell.* 21:3362–3375. http://dx.doi.org/10.1091/mbc.E10-02-0094

Carlier, M.F., J. Pernier, P. Montaville, S. Shekhar, and S. Kühn. Cytoskeleton Dynamics and Motility group. 2015. Control of polarized assembly of actin filaments in cell motility. *Cell. Mol. Life Sci.* 72:3051–3067. http://dx.doi.org/10.1007/s00018-015-1914-2

Chan, W., R. Kozma, Y. Yasui, M. Inagaki, T. Leung, E. Manser, and L. Lim. 2002. Vimentin intermediate filament reorganization by Cdc42: involvement of PAK and p70 S6 kinase. *Eur. J. Cell Biol.* 81:692–701. http://dx.doi.org/10.1078/0171-9335-00281

Chu, Y., S. Hughes, and T. Chan-Ling. 2001. Differentiation and migration of astrocyte precursor cells and astrocytes in human fetal retina: relevance to optic nerve coloboma. *FASEB J.* 15:2013–2015.

Çolakoğlu, G., and A. Brown. 2009. Intermediate filaments exchange subunits along their length and elongate by end-to-end annealing. *J. Cell Biol.* 185:769–777. http://dx.doi.org/10.1083/jcb.200809166

Dujardin, D.L., L.E. Barnhart, S.A. Stehman, E.R. Gomes, G.G. Gundersen, and R.B. Vallee. 2003. A role for cytoplasmic dynein and LIS1 in directed cell movement. *J. Cell Biol.* 163:1205–1211. http://dx.doi.org/10.1083/jcb.200310097

Dupin, I., and S. Etienne-Manneville. 2011. Nuclear positioning: mechanisms and functions. *Int. J. Biochem. Cell Biol.* 43:1698–1707. http://dx.doi.org/10.1016/j.biocel.2011.09.004

Dupin, I., E. Camand, and S. Etienne-Manneville. 2009. Classical cadherins control nucleus and centrosome position and cell polarity. *J. Cell Biol.* 185:779–786. http://dx.doi.org/10.1083/jcb.200812034

Dupin, I., Y. Sakamoto, and S. Etienne-Manneville. 2011. Cytoplasmic intermediate filaments mediate actin-driven positioning of the nucleus. *J. Cell Sci.* 124:865–872. http://dx.doi.org/10.1242/jcs.076356

Dupin, I., J. Elric, and S. Etienne-Manneville. 2015. Adhesive micropatterns to study intermediate filament function in nuclear positioning. *Curr. Protoc. Cell Biol.* 66:1–19. http://dx.doi.org/10.1002/0471143030.cb1307s66

Eliasson, C., C. Sahlgren, C.H. Berthold, J. Stakeberg, J.E. Celis, C. Betsholtz, J.E. Eriksson, and M. Pekny. 1999. Intermediate filament protein partnership in astrocytes. *J. Biol. Chem.* 274:23996–24006. http://dx.doi.org/10.1074/jbc.274.34.23996

Etienne-Manneville, S. 2004. Cdc42 - the centre of polarity. *J. Cell Sci.* 117:1291–1300. http://dx.doi.org/10.1242/jcs.01115

Etienne-Manneville, S. 2006. *In vitro* assay of primary astrocyte migration as a tool to study Rho GTPase function in cell polarization. *Methods Enzymol.* 406:565–578. http://dx.doi.org/10.1016/S0076-6879(06)06044-7

Etienne-Manneville, S. 2008. Polarity proteins in migration and invasion. *Oncogene.* 27:6970–6980. http://dx.doi.org/10.1038/onc.2008.347

Etienne-Manneville, S. 2013. Microtubules in cell migration. *Annu. Rev. Cell Dev. Biol.* 29:471–499. http://dx.doi.org/10.1146/annurev-cellbio-101011-155711

Etienne-Manneville, S., and A. Hall. 2001. Integrin-mediated activation of Cdc42 controls cell polarity in migrating astrocytes through PKCζ. *Cell.* 106:489–498. http://dx.doi.org/10.1016/S0092-8674(01)00471-8

Etienne-Manneville, S., and A. Hall. 2002. Rho GTPases in cell biology. *Nature.* 420:629–635. http://dx.doi.org/10.1038/nature01148

Etienne-Manneville, S., and A. Hall. 2003. Cell polarity: Par6, aPKC and cytoskeletal crosstalk. *Curr. Opin. Cell Biol.* 15:67–72. http://dx.doi.org/10.1016/S0955-0674(02)00005-4

Etienne-Manneville, S., J.B. Manneville, S. Nicholls, M.A. Ferenczi, and A. Hall. 2005. Cdc42 and Par6–PKCζ regulate the spatially localized association of Dlg1 and APC to control cell polarization. *J. Cell Biol.* 170:895–901. http://dx.doi.org/10.1083/jcb.200412172

Faber-Elman, A., A. Solomon, J.A. Abraham, M. Marikovsky, and M. Schwartz. 1996. Involvement of wound-associated factors in rat brain astrocyte migratory response to axonal injury: in vitro simulation. *J. Clin. Invest.* 97:162–171. http://dx.doi.org/10.1172/JCI118385

Fruttiger, M. 2002. Development of the mouse retinal vasculature: angiogenesis versus vasculogenesis. *Invest. Ophthalmol. Vis. Sci.* 43:522–527.

Gan, Z., L. Ding, C.J. Burckhardt, J. Lowery, A. Zaritsky, K. Sitterley, A. Mota, N. Costigliola, C.G. Starker, D.F. Voytas, et al. 2016. Vimentin intermediate filaments template microtubule networks to enhance persistence in cell polarity and directed migration. *Cell Syst.* 3:252–263.

Gao, Y., J.B. Dickerson, F. Guo, J. Zheng, and Y. Zheng. 2004. Rational design and characterization of a Rac GTPase-specific small molecule inhibitor. *Proc. Natl. Acad. Sci. USA.* 101:7618–7623. http://dx.doi.org/10.1073/pnas.0307512101

Gnanaguru, G., G. Bachay, S. Biswas, G. Pinzón-Duarte, D.D. Hunter, and W.J. Brunken. 2013. Laminins containing the β2 and γ3 chains regulate astrocyte migration and angiogenesis in the retina. *Development.* 140:2050–2060. http://dx.doi.org/10.1242/dev.087817

Goldman, R.D. 1971. The role of three cytoplasmic fibers in BHK-21 cell motility. *J. Cell Biol.* 51:752–762. http://dx.doi.org/10.1083/jcb.51.3.752

Gregor, M., S. Osmanagic-Myers, G. Burgstaller, M. Wolfram, I. Fischer, G. Walko, G.P. Resch, A. Jörgl, H. Herrmann, and G. Wiche. 2014. Mechanosensing through focal adhesion-anchored intermediate filaments. *FASEB J.* 28:715–729. http://dx.doi.org/10.1096/fj.13-231829

Gyoeva, F.K., and V.I. Gelfand. 1991. Coalignment of vimentin intermediate filaments with microtubules depends on kinesin. *Nature.* 353:445–448. http://dx.doi.org/10.1038/353445a0

Hancock, W.O. 2014. Bidirectional cargo transport: moving beyond tug of war. *Nat. Rev. Mol. Cell Biol.* 15:615–628. http://dx.doi.org/10.1038/nrm3853

Helfand, B.T., A. Mikami, R.B. Vallee, and R.D. Goldman. 2002. A requirement for cytoplasmic dynein and dynactin in intermediate filament network assembly and organization. *J. Cell Biol.* 157:795–806. http://dx.doi.org/10.1083/jcb.200202027

Helfand, B.T., M.G. Mendez, S.N.P. Murthy, D.K. Shumaker, B. Grin, S. Mahammad, U. Aebi, T. Wedig, Y.I. Wu, K.M. Hahn, et al. 2011. Vimentin organization modulates the formation of lamellipodia. *Mol. Biol. Cell.* 22:1274–1289. http://dx.doi.org/10.1091/mbc.E10-08-0699

Herrmann, H., and U. Aebi. 2000. Intermediate filaments and their associates: multi-talented structural elements specifying cytoarchitecture and cytodynamics. *Curr. Opin. Cell Biol.* 12:79–90. http://dx.doi.org/10.1016/S0955-0674(99)00060-5

Hol, E.M., and M. Pekny. 2015. Glial fibrillary acidic protein (GFAP) and the astrocyte intermediate filament system in diseases of the central nervous system. *Curr. Opin. Cell Biol.* 32:121–130. http://dx.doi.org/10.1016/j.ceb.2015.02.004

Hollenbeck, P.J., A.D. Bershadsky, O.Y. Pletjushkina, I.S. Tint, and J.M. Vasiliev. 1989. Intermediate filament collapse is an ATP-dependent and actin-dependent process. *J. Cell Sci.* 92:621–631.

Hong, L., S.R. Kenney, G.K. Phillips, D. Simpson, C.E. Schroeder, J. Nöth, E. Romero, S. Swanson, A. Waller, J.J. Strouse, et al. 2013. Characterization of a Cdc42 protein inhibitor and its use as a molecular probe. *J. Biol. Chem.* 288:8531–8543. http://dx.doi.org/10.1074/jbc.M112.435941

Hookway, C., L. Ding, M.W. Davidson, J.Z. Rappoport, G. Danuser, and V.I. Gelfand. 2015. Microtubule-dependent transport and dynamics of vimentin intermediate filaments. *Mol. Biol. Cell.* 26:1675–1686. http://dx.doi.org/10.1091/mbc.E14-09-1398

Huber, F., A. Boire, M.P. López, and G.H. Koenderink. 2015. Cytoskeletal crosstalk: when three different personalities team up. *Curr. Opin. Cell Biol.* 32:39–47. http://dx.doi.org/10.1016/j.ceb.2014.10.005

Ilhan-Mutlu, A., L. Wagner, G. Widhalm, A. Wohrer, S. Bartsch, T. Czech, H. Heinzl, F. Leutmezer, D. Prayer, C. Marosi, et al. 2013. Exploratory investigation of eight circulating plasma markers in brain tumor patients. *Neurosurg. Rev.* 36:45.

Jiu, Y., J. Lehtimäki, S. Tojkander, F. Cheng, H. Jäälinoja, X. Liu, M. Varjosalo, J.E. Eriksson, and P. Lappalainen. 2015. Bidirectional interplay between vimentin intermediate filaments and contractile actin stress fibers. *Cell Reports.* 11:1511–1518. http://dx.doi.org/10.1016/j.celrep.2015.05.008

Jung, T.Y., and S. Jung. 2007. Early neuroimaging findings of glioblastoma mimicking non-neoplastic cerebral lesion. *Neurol. Med. Chir. (Tokyo).* 47:424–427. http://dx.doi.org/10.2176/nmc.47.424

Kölsch, A., R. Windoffer, and R.E. Leube. 2009. Actin-dependent dynamics of keratin filament precursors. *Cell Motil. Cytoskeleton.* 66:976–985. http://dx.doi.org/10.1002/cm.20395

Kölsch, A., R. Windoffer, T. Würflinger, T. Aach, and R.E. Leube. 2010. The keratin-filament cycle of assembly and disassembly. *J. Cell Sci.* 123:2266–2272. http://dx.doi.org/10.1242/jcs.068080

Köster, D.V., and S. Mayor. 2016. Cortical actin and the plasma membrane: inextricably intertwined. *Curr. Opin. Cell Biol.* 38:81–89. http://dx.doi.org/10.1016/j.ceb.2016.02.021

Kozma, R., S. Ahmed, A. Best, and L. Lim. 1995. The Ras-related protein Cdc42Hs and bradykinin promote formation of peripheral actin microspikes and filopodia in Swiss 3T3 fibroblasts. *Mol. Cell. Biol.* 15:1942–1952. http://dx.doi.org/10.1128/MCB.15.4.1942

Ladoux, B., R.M. Mège, and X. Trepat. 2016. Front–rear polarization by mechanical cues: From single cells to tissues. *Trends Cell Biol.* 26:420–433. http://dx.doi.org/10.1016/j.tcb.2016.02.002

Leduc, C., and S. Etienne-Manneville. 2015. Intermediate filaments in cell migration and invasion: the unusual suspects. *Curr. Opin. Cell Biol.* 32:102–112. http://dx.doi.org/10.1016/j.ceb.2015.01.005

Lepekhin, E.A., C. Eliasson, C.H. Berthold, V. Berezin, E. Bock, and M. Pekny. 2001. Intermediate filaments regulate astrocyte motility. *J. Neurochem.* 79:617–625. http://dx.doi.org/10.1046/j.1471-4159.2001.00595.x

Liao, G., and G.G. Gundersen. 1998. Kinesin is a candidate for cross-bridging microtubules and intermediate filaments. Selective binding of kinesin to detyrosinated tubulin and vimentin. *J. Biol. Chem.* 273:9797–9803. http://dx.doi.org/10.1074/jbc.273.16.9797

Llense, F., and S. Etienne-Manneville. 2015. Front-to-rear polarity in migrating cells. *In* Cell polarity. Vol. 1. K. Ebnet, editor. Springer, New York. 115–146.

Lynch, C.D., A.M. Lazar, T. Iskratsch, X. Zhang, and M.P. Sheetz. 2013. Endoplasmic spreading requires coalescence of vimentin intermediate filaments at force-bearing adhesions. *Mol. Biol. Cell.* 24:21–30. http://dx.doi.org/10.1091/mbc.E12-05-0377

Manneville, J.B., M. Jehanno, and S. Etienne-Manneville. 2010. Dlg1 binds GKAP to control dynein association with microtubules, centrosome positioning, and cell polarity. *J. Cell Biol.* 191:585–598. http://dx.doi.org/10.1083/jcb.201002151

Maslehaty, H., S. Cordovi, and M. Hefti. 2011. Symptomatic spinal metastases of intracranial glioblastoma: clinical characteristics and pathomechanism relating to GFAP expression. *J. Neurooncol.* 101:329–333. http://dx.doi.org/10.1007/s11060-010-0257-y

Meriane, M., S. Mary, F. Comunale, E. Vignal, P. Fort, and C. Gauthier-Rouviére. 2000. Cdc42Hs and Rac1 GTPases induce the collapse of the vimentin intermediate filament network. *J. Biol. Chem.* 275:33046–33052. http://dx.doi.org/10.1074/jbc.M001566200

Murray, M.E., M.G. Mendez, and P.A. Janmey. 2014. Substrate stiffness regulates solubility of cellular vimentin. *Mol. Biol. Cell.* 25:87–94. http://dx.doi.org/10.1091/mbc.E13-06-0326

Osmani, N., N. Vitale, J.P. Borg, and S. Etienne-Manneville. 2006. Scrib controls Cdc42 localization and activity to promote cell polarization during astrocyte migration. *Curr. Biol.* 16:2395–2405. http://dx.doi.org/10.1016/j.cub.2006.10.026

Osmani, N., F. Peglion, P. Chavrier, and S. Etienne-Manneville. 2010. Cdc42 localization and cell polarity depend on membrane traffic. *J. Cell Biol.* 191:1261–1269. http://dx.doi.org/10.1083/jcb.201003091

Palazzo, A.F., H.L. Joseph, Y.J. Chen, D.L. Dujardin, A.S. Alberts, K.K. Pfister, R.B. Vallee, and G.G. Gundersen. 2001. Cdc42, dynein, and dynactin regulate MTOC reorientation independent of Rho-regulated microtubule stabilization. *Curr. Biol.* 11:1536–1541. http://dx.doi.org/10.1016/S0960-9822(01)00475-4

Peglion, F., F. Llense, and S. Etienne-Manneville. 2014. Adherens junction treadmilling during collective migration. *Nat. Cell Biol.* 16:639–651. http://dx.doi.org/10.1038/ncb2985

Peterson, J.R., L.C. Bickford, D. Morgan, A.S. Kim, O. Ouerfelli, M.W. Kirschner, and M.K. Rosen. 2004. Chemical inhibition of N-WASP by stabilization of a native autoinhibited conformation. *Nat. Struct. Mol. Biol.* 11:747–755. http://dx.doi.org/10.1038/nsmb796

Prahlad, V., M. Yoon, R.D. Moir, R.D. Vale, and R.D. Goldman. 1998. Rapid movements of vimentin on microtubule tracks: Kinesin-dependent assembly of intermediate filament networks. *J. Cell Biol.* 143:159–170. http://dx.doi.org/10.1083/jcb.143.1.159

Ridley, A.J. 2015. Rho GTPase signalling in cell migration. *Curr. Opin. Cell Biol.* 36:103–112. http://dx.doi.org/10.1016/j.ceb.2015.08.005

Robert, A., H. Herrmann, M.W. Davidson, and V.I. Gelfand. 2014. Microtubule-dependent transport of vimentin filament precursors is regulated by actin and by the concerted action of Rho- and p21-activated kinases. *FASEB J.* 28:2879–2890.

Robert, A., C. Hookway, and V.I. Gelfand. 2016. Intermediate filament dynamics: What we can see now and why it matters. *BioEssays.* 38:232–243. http://dx.doi.org/10.1002/bies.201500142

Rossé, C., C. Lodillinsky, L. Fuhrmann, M. Nourieh, P. Monteiro, M. Irondelle, E. Lagoutte, S. Vacher, F. Waharte, P. Paul-Gilloteaux, et al. 2014. Control of MT1-MMP transport by atypical PKC during breast-cancer progression. *Proc. Natl. Acad. Sci. USA.* 111:E1872–E1879. http://dx.doi.org/10.1073/pnas.1400749111

Sakamoto, Y., B. Boëda, and S. Etienne-Manneville. 2013. APC binds intermediate filaments and is required for their reorganization during cell migration. *J. Cell Biol.* 200:249–258. http://dx.doi.org/10.1083/jcb.201206010

Schindelin, J., I. Arganda-Carreras, E. Frise, V. Kaynig, M. Longair, T. Pietzsch, S. Preibisch, C. Rueden, S. Saalfeld, B. Schmid, et al. 2012. Fiji: an open-source platform for biological-image analysis. *Nat. Methods.* 9:676–682. http://dx.doi.org/10.1038/nmeth.2019

Shabbir, S.H., M.M. Cleland, R.D. Goldman, and M. Mrksich. 2014. Geometric control of vimentin intermediate filaments. *Biomaterials.* 35:1359–1366. http://dx.doi.org/10.1016/j.biomaterials.2013.10.008

Skalli, O., U. Wilhelmsson, C. Orndahl, B. Fekete, K. Malmgren, B. Rydenhag, and M. Pekny. 2013. Astrocytoma grade IV (glioblastoma multiforme) displays 3 subtypes with unique expression profiles of intermediate filament proteins. *Hum. Pathol.* 44:2081–2088. http://dx.doi.org/10.1016/j.humpath.2013.03.013

Sofroniew, M.V. 2009. Molecular dissection of reactive astrogliosis and glial scar formation. *Trends Neurosci.* 32:638–647. http://dx.doi.org/10.1016/j.tins.2009.08.002

Steinert, P.M., Y.H. Chou, V. Prahlad, D.A. Parry, L.N. Marekov, K.C. Wu, S.I. Jang, and R.D. Goldman. 1999a. A high molecular weight intermediate filament-associated protein in BHK-21 cells is nestin, a type VI intermediate filament protein. Limited co-assembly *in vitro* to form heteropolymers with type III vimentin and type IV α-internexin. *J. Biol. Chem.* 274:9881–9890. http://dx.doi.org/10.1074/jbc.274.14.9881

Steinert, P.M., L.N. Marekov, and D.A. Parry. 1999b. Molecular parameters of type IV α-internexin and type IV-type III α-internexin-vimentin copolymer intermediate filaments. *J. Biol. Chem.* 274:1657–1666. http://dx.doi.org/10.1074/jbc.274.3.1657

Sultana, S., S.W. Sernett, R.M. Bellin, R.M. Robson, and O. Skalli. 2000. Intermediate filament protein synemin is transiently expressed in a subset of astrocytes during development. *Glia.* 30:143–153. http://dx.doi.org/10.1002/(SICI)1098-1136(200004)30:2<143::AID-GLIA4>3.0.CO;2-Z

Svitkina, T.M., A.B. Verkhovsky, and G.G. Borisy. 1996. Plectin sidearms mediate interaction of intermediate filaments with microtubules and other components of the cytoskeleton. *J. Cell Biol.* 135:991–1007. http://dx.doi.org/10.1083/jcb.135.4.991

Théry, M. 2010. Micropatterning as a tool to decipher cell morphogenesis and functions. *J. Cell Sci.* 123:4201–4213. http://dx.doi.org/10.1242/jcs.075150

Uchida, A., G. Çolakoğlu, L. Wang, P.C. Monsma, and A. Brown. 2013. Severing and end-to-end annealing of neurofilaments in neurons. *Proc. Natl. Acad. Sci. USA.* 110:E2696–E2705. http://dx.doi.org/10.1073/pnas.1221835110

Walczak, C.E., R.S. Rizk, and S.L. Shaw. 2010. The use of fluorescence redistribution after photobleaching for analysis of cellular microtubule dynamics. *Methods Cell Biol.* 97:35–52. http://dx.doi.org/10.1016/S0091-679X(10)97003-9

Wickert, U., N. Mücke, T. Wedig, S.A. Müller, U. Aebi, and H. Herrmann. 2005. Characterization of the in vitro co-assembly process of the intermediate filament proteins vimentin and desmin: mixed polymers at all stages of assembly. *Eur. J. Cell Biol.* 84:379–391. http://dx.doi.org/10.1016/j.ejcb.2005.01.004

Zegers, M.M., and P. Friedl. 2014. Rho GTPases in collective cell migration. *Small GTPases.* 5:e983869. http://dx.doi.org/10.4161/sgtp.28997